DOI 10.24425/aee.2026.7061

Multi-terminal electric vehicle fast-charging station based on current-fed multi-active bridge converter

MYKOLA LUKIANOV [1]✉, ENRIQUE ROMERO CADAVAL [2], OLEKSANDR MATIUSHKIN [3], JAKUB GOZDEK [4], RYSZARD STRZELECKI [4]

[1] *Faculty of Electrical and Control Engineering, Gdańsk University of Technology Gabriela Narutowicza 11/12, 80-233 Gdańsk, Poland*

[2] *Power Electrical and Electronic Systems R+D Group, University of Extremadura Av. de Elvas, s/n, 06006 Badajoz, Spain*

[3] *FinEst Centre for Smart Cities, Tallinn University of Technology Ehitajate tee 5, 12616 Tallinn, Estonia*

[4] *Faculty of Electrical Engineering, Gdynia Maritime University Morska 81/87, 81-225 Gdynia, Poland*

e-mail: ✉ *mykola.lukianov@pg.edu.pl, eromero@unex.ex, oleksandr.matiushkin@taltech.ee, jakub.gozdek@outlook.com, r.strzelecki@we.umg.edu.pl*

(Received: 01.09.2026, revised: 19.10.2026)

Abstract: The number of fully electric vehicles (EVs) on the road is continuously increasing year by year, creating a growing demand for multi-terminal EV charging infrastructure, where multiple charging terminals serving different EVs are located in close proximity. Many existing multi-terminal fast EV charging stations are based on architectures with multiple independent or modular power conversion units, in which each charging outlet requires dedicated power conversion hardware. Consequently, as the number of charging outlets increases, the amount of required hardware (semiconductors, passive components, processors, etc.) scales approximately linearly, leading to a corresponding increase in the overall cost of the charging station. As a potential solution to reduce the installation cost of multi-terminal EV charging stations, this article presents a multiport current-fed multi-active bridge (CF-MAB) converter that requires fewer components while maintaining independent port operation and enabling the integration of a battery energy storage system. In the proposed application, the CF-MAB is connected to a low-voltage DC traction grid, allowing the shared use of existing traction substation equipment, such as the low-frequency transformer and AC/DC rectifier, for both electric traction and EV charging. This approach further reduces infrastructure costs by eliminating the need for a dedicated transformer and AC/DC rectifier at the charging station. A reduced scale five-port CF-MAB prototype was experimentally evaluated under various operating conditions with a power rating of up to 10 kW, achieving a peak efficiency of up to 98%.



© 2026. The Author(s). This is an open-access article distributed under the terms of the Creative Commons Attribution-NonCommercial-NoDerivatives License (CC BY-NC-ND 4.0, https://creativecommons.org/licenses/by-nc-nd/4.0/), which permits use, distribution, and reproduction in any medium, provided that the Article is properly cited, the use is non-commercial, and no modifications or adaptations are made.

Key words: bidirectional converter, current-fed active bridge, fast EV charger, multiport DC–DC converter, traction grids

1. Introduction

The rapid expansion of DC power systems such as electric vehicle (EV) chargers, battery energy storage systems (BESs) and renewable energy sources (RESs) has led to a growing demand for bidirectional DC–DC converters capable of managing power flow between various DC sources and loads [1]. Traditionally, RES, BES and EV chargers are connected to DC grids using independent isolated and non-isolated converters [2]. Such solutions offer simplicity, modularity and high reliability. However, they require a large number of components and result in longer energy conversion paths during power exchange between individual units. In systems where multiple sources and loads must be interconnected simultaneously, usage of multiport DC–DC converters represents a more cost-effective and efficient alternative [3].

This paper therefore presents a bidirectional DC–DC converter for integrating BES and electric vehicle (EV) chargers into a low-voltage DC traction grid used to supply urban tram and trolleybus networks (Fig. 1).

By sharing power components among multiple ports, the studied converter achieves a reduced component count and high efficiency, making it a promising solution for DC grid applications.

One promising application of the proposed topology is public multi-terminal EV charging stations installed near urban rail transport infrastructure. In such locations, the available power capacity of traction substations can be utilized for EV charging, since these substations frequently operate below their rated power due to discontinuous operation of trams and trolleybuses, particularly during periods of low traffic, such as nighttime [4]. In the considered system, the BES primarily serves to recuperate braking energy, thereby improving the energy efficiency of traction transport and stabilizing the DC grid voltage. Additionally, the BES operates as a buffer battery to support EV charging when required.

The electrical operating conditions of the proposed charging station are subject to the standardization requirements applicable to DC traction networks. According to EN 50163 [5], a nominal 600 V DC traction system is characterized by a wide permissible voltage range, with the lowest permanent voltage of 400 V and the highest permanent voltage of 720 V, while the maximum non-permanent voltage reaches 770 V. Therefore, a power electronic interface connected to such a network must accommodate considerable variations of its input voltage. In addition to the voltage limits, the interaction of power electronic equipment with the traction network requires consideration of power-flow limitation, regenerative operation, protection coordination and electromagnetic compatibility. EN 50388-1 [6] specifies, among others, automatic current or power limitation as a function of the line voltage, coordination of short-circuit protection and the use of regenerative braking. These aspects are particularly relevant to the proposed charging station, since the CF-MAB provides bidirectional power transfer and its high-level controller determines the charging and discharging limits of the BES and EV ports from the measured catenary voltage. Furthermore, fixed power-electronic equipment connected to traction power conductors is subject to the emission and immunity considerations specified in EN 50121-5. Consequently, practical deployment of the proposed converter would additionally require appropriate input protection, EMC filtering and coordination with the protection and earthing arrangements of the particular traction network.

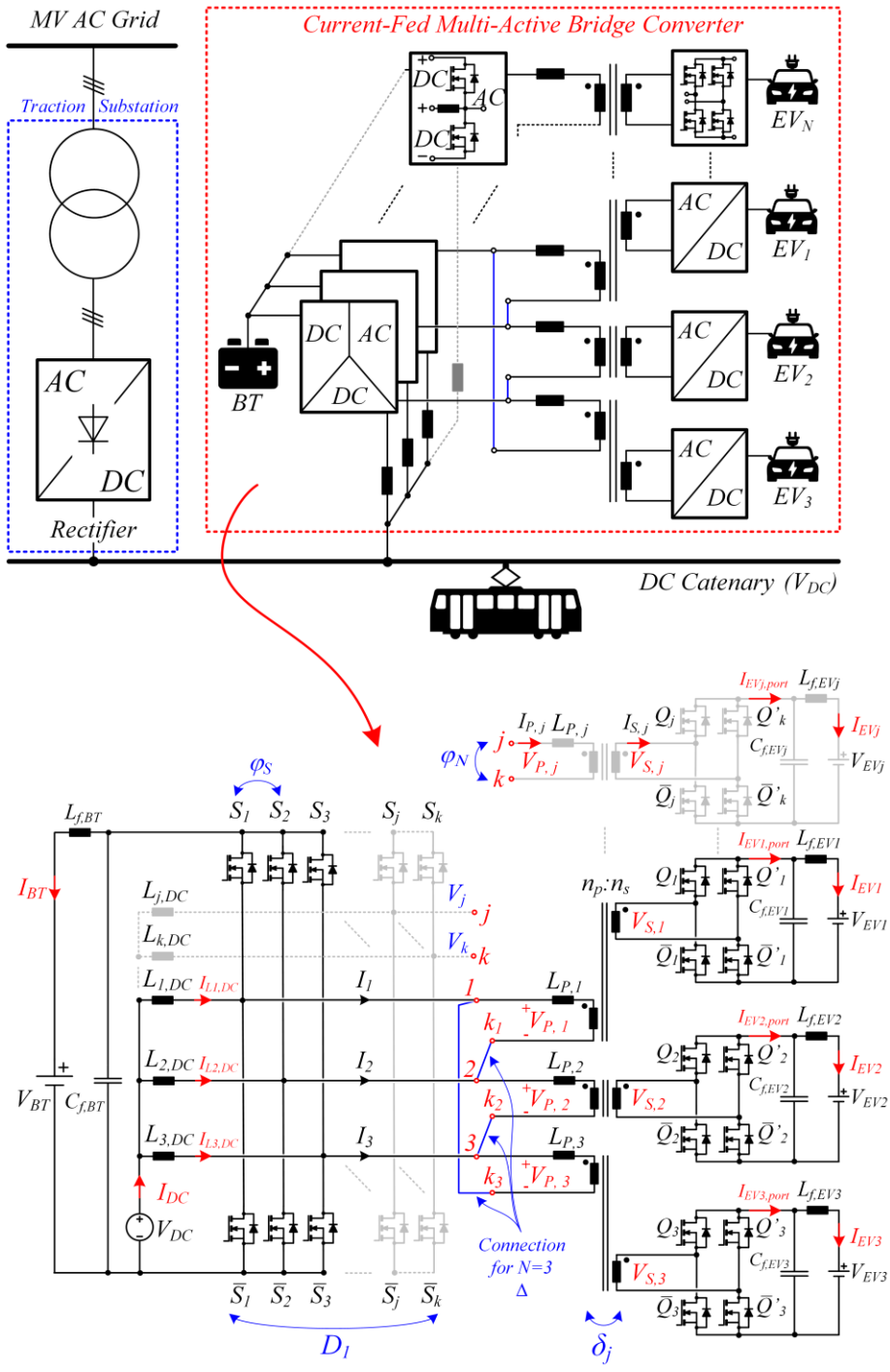


Fig. 1. Multiterminal charging station based on the studied CF-MAB converter, powered from an LV DC traction grid

Among existing multiport solutions, the studied CF-MAB converter can be compared to the multi-active bridge (MAB) converter, the structure of which has several active bridges, all coupled with a common core transformer, e.g. triple active bridge (TAB) or quad active bridge (QAB) [7]. These converters require a relatively low number of switches, but strong coupling between ports leads to complex control [8]. This is particularly problematic in applications with a high number of ports, where each output operates at different voltage and power levels, which is a common case for a multiport EV charging station. To address the port interdependence issue, MAB converters with single-phase transformers were proposed [9], enabling decoupled control of multiple -EV charging, while maintaining a lower switch count. Nevertheless, its connection to a fluctuating DC traction grid complicates EV charging, increasing the converter design complexity and technical requirements, which, in many cases, result in a less optimized converter. To eliminate the voltage mismatch between the varying DC traction grid voltage and the EV battery voltage, the current-fed dual active bridge (CF-DAB) converter family can be used [10]. The classical single-phase CF-DAB converter has a structure similar to that of a conventional DAB converter, but includes two additional boost inductors connected to the switching nodes of the primary-side half bridges, thereby forming a boost stage. As a result, the input voltage can be boosted, stabilized and regulated across the auxiliary DC-link capacitor y changing the primary-side switches duty cycle. Consequently, optimal matching between the auxiliary DC-link capacitor voltage and the EV battery voltage can be achieved, improving the converter performance. However, both single-phase [11] and multi-phase CF-DAB converters [12] have limited scalability, typically providing only three connection ports. As a result, multiple CF-DAB converters are required for a multi-terminal charging station, similarly to conventional DAB-based solutions, leading to a high overall switch count and increased system complexity.

To address the aforementioned limitations, a current-fed multi-active bridge (CF-MAB) topology was proposed by authors of this article in [13]. The proposed topology integrates the benefits of the single-phase transformer-based MAB converter [9] with selected features of the CF-DAB converter [12]. As a result, the CF-MAB converter allows the integration of multiple isolated EV charging ports N, incorporates separate interfaces for the DC grid and the battery energy storage system, while providing fully independent and bidirectional power transfer among all connected ports, thereby supporting vehicle-to-grid (V2G) functionality.

Section 2 discusses the CF-MAB converter structure and presents analytical expressions for component RMS currents calculation and magnetics design. Section III outlines the converter control algorithm, while Section IV presents experimental results obtained from a 10kW five-port prototype, including three EV charging ports, one BES port and one DC grid connection port.

2. CF-MAB converter topology description

2.1. CF-MAB converter structure

The input side of the converter operates similarly to a N-phase interleaved boost converter, the phases of which are shifted relative to each other by angle $\varphi_S = 2\pi/N$, where $N = 3, 5 \ldots$ The DC traction grid voltage has to be lower than the battery voltage V_{BT} for the converter to operate.

Switches S_1, ..., S_N are driven with a duty cycle of D_1, determined according to (1), while the complementary switches S_{Z1}, ..., S_{ZN} operate with a duty cycle $1 - D_1$.

$$D_1 = \frac{T_S}{T} = \frac{V_{DC}}{V_{BT}}. \tag{1}$$

The isolated EV charging ports comprise of N identical full-bridges, isolated by single-phase transformers, which are connected on the primary side to the half-bridge switching nodes with indexes "j" and "k", defined as:

$$k = \left(j + \frac{N-1}{2}\right) - N \cdot \left\lfloor \frac{2j + N - 2}{2N} \right\rfloor, \tag{2}$$

where: $j = 1, 2, \ldots, N$; $\lfloor \cdot \rfloor$ – floor function.

Voltages V_j and V_k, formed at switching points, indexed as "j" and "k" are phase-shifted relative to each other by $\varphi_N = \pi(N-1)/N$ (Fig. 2). This results in a transformer primary side windings being connected in a delta (Δ) connection, when the number of isolated ports is equal to $N = 3$. The phase shift between the primary switches in such a case is equal to $\varphi_S = \varphi_N = 2\pi/3$. To control the output-port power, phase shifts δ_j between transformer primary $V_{P,j}$ and secondary side $V_{S,j}$ voltages of each EV port are controlled independently. As a result, the operation of each EV port resembles that of an independent single-phase DAB converter, comprising the primary-side switches S_j, S'_j, S_k, S'_k and the secondary-side switches Q_j, Q'_j, Q''_j, Q'''_j.

When operating with single-phase shift (SPS) modulation, the secondary side full-bridge is phase-shifted by δ_j, such that Q_j referenced to S_j and Q'_j to S_k. Accordingly, the CF-MAB converter may be viewed as an integration of an N-phase interleaved boost converter and N individual active bridge converters with shared input-side switches. It is worth mentioning that in a CF-MAB converter, phase-to-phase voltages $V_{P,j}$, exhibit unequal zero-voltage intervals preceding and following the active voltage pulses, with their duration determined by D_1 and φ_N (Fig. 2). The presence of these zero-voltage intervals reduces transformer utilization, since no power is transferred to the output during a considerable portion of the switching period.

In contrast to the conventional DAB converter, the CF-MAB topology cannot employ triple-phase-shift (TPS) modulation because the phase φ_N between the primary-side bridges is fixed. This means that varying φ_N disrupts the interleaving of the primary-side phases, resulting in increased current ripple, whereas adjusting D_1 directly affects the battery current I_{BT}. Therefore, only two independent control variables remain for regulating each isolated port: the secondary-side pulse width $d_{S,j}$ and the phase shift δ_j between the primary- and secondary-side voltages. Under these constraints, a modified dual-phase-shift (DPS) modulation scheme operating with $D_1 \neq 0.5$ provides a practical solution for maintaining volt-second balance, satisfying $nV_{BT} \cdot d_{P,j} = V_{EV} \cdot d_{S,j}$ while simultaneously reducing transformer RMS currents as the EV battery voltage varies during the charging process [14].

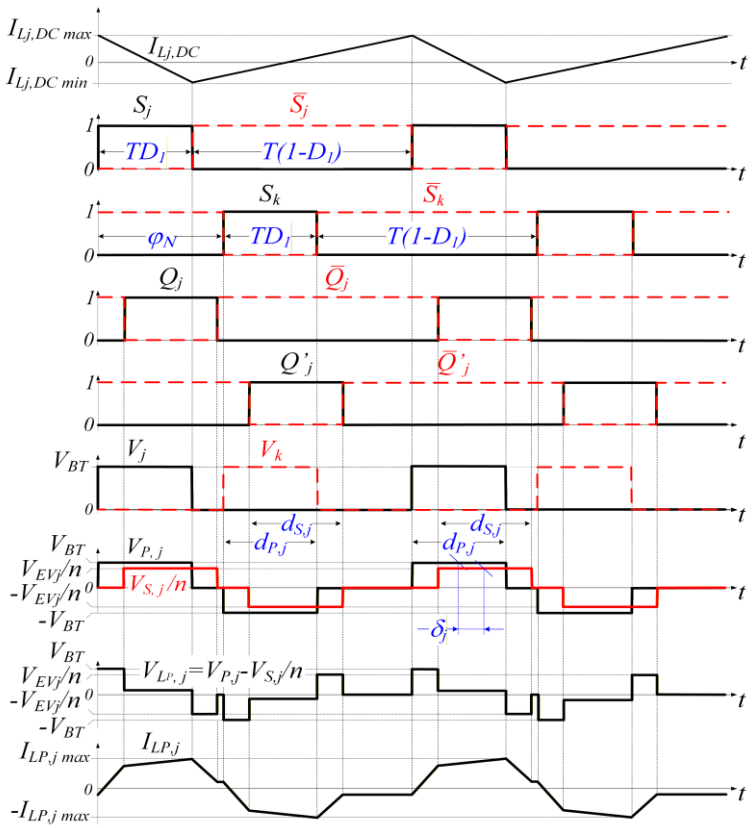


Fig. 2. CF-MAB converter operating diagrams with SPS modulation

2.2. Components RMS currents derivation

The following formulas describe RMS currents for a CF-MAB converter operating with SPS modulation, where $d_{S,j} = d_{P,j}$:

$$I_{\overline{S}j}\text{rms} = \sqrt{\frac{1}{T}\int_0^{T(1-D_1)-\alpha} \left(I_{Lj,\text{DC}}(t) - I_j(t)\right)^2 \text{d}t},$$
$$I_{Sj}\text{rms} = \sqrt{\frac{1}{T}\int_{T(1-D_1)-\alpha}^{T-\alpha} \left(I_{Lj,\text{DC}}(t) - I_j(t)\right)^2 \text{d}t}, \tag{3}$$

where $I_j(t) = I_{LP,j}(t) - I_{LP,k+1}(t)$ is a line current.

Primary-side switch currents have quite complex shape, as they have to carry current of the primary-side inductors $I_{\text{L}j,\text{DC}}(t)$ and line currents $I_j(t)$. Line currents $I_j(t)$ in turn, depend on the phase currents $I_{LP,j}(t)$ and $I_{LP,k+1}(t)$, which can be represented by a Fourier series:

$$
\begin{aligned}
I_{LP,j}(t) &= \sum\nolimits_{m=1,2,3,\ldots} \frac{2}{m^2\omega_0\pi L_{P,j}} \left[\sqrt{A^2 - 2AB\cos(m\omega_0\delta_j) + B^2}\cdot\cos(m\omega_0 t + \phi)\right], \\
A &= V_{\mathrm{BT}}\left[\cos(m(\alpha + d_{P,j})) - \cos(m\alpha)\right], \\
B &= \frac{V_{\mathrm{EV},j}}{n}\left[\cos(m(\alpha + d_{S,j})) - \cos(m\alpha)\right], \\
\phi &= \arctan\left(\frac{B\sin(m\omega_0\delta_j)}{A - B\cos(m\omega_0\delta_j)}\right),
\end{aligned}
\tag{4}
$$

where α, $d_{P,j}$ and $d_{S,j}$ are calculated for different converter operation regions:

$D_1 < 1/3$:	$1/3 \le D_1 \le 2/3$:	$D_1 > 2/3$:
$\alpha = T/3 - d_{P,j}$ $d_{S,j} = d_{P,j} = TD_1$	$\alpha = \frac{1}{2}(D_1 - T/3)$ $d_{S,j} = d_{P,j} = T/3$	$\alpha = T - D_1$ $d_{S,j} = d_{P,j} = T(1 - D_1)$

As can be seen, the phase currents $I_{LP,j}(t)$ for each port depend on their own phase shift δ_j and the voltage level V_{EV_j} of the EVs connected to the ports. In contrast α, $d_{P,j}$ and $d_{S,j}$ are the same for all ports ($d_{P,1} = d_{P,2} = d_{P,3} = d_{S,1} = d_{S,2} = d_{S,3}$), as they depend on the primary side duty cycle D_1, which is common to all ports (this is true only for SPS modulation; for modified DPS modulation see reference [14]). Different phase currents $I_{LP,j}(t)$ imply that line currents $I_j(t)$ are also different. Consequently, this decreases switch RMS current when $I_j(t)$ is positive and increases switch RMS current when $I_j(t)$ is negative (when S_j is turned ON). As a result, the current distribution, waveform shapes and RMS currents in primary side switches S_j, S'_j, S_k, S'_k are different as well. On the other hand, if variables are the same $\delta_1 = \delta_2 = \delta_3$, $V_{\mathrm{EV},1} = V_{\mathrm{EV},2} = V_{\mathrm{EV},3}$, RMS currents in all switches are also the same.

As the current of the output switches is determined by the $I_{LP,j}(t)$, and since two switches conduct for only half of the switching period, their RMS current is defined as:

$$
I_{Qj}\mathrm{rms} = I_{Q'j}\mathrm{rms} = \frac{I_{LP,j}\mathrm{rms}}{n\cdot\sqrt{2}}. \tag{5}
$$

Primary side boost inductors $I_{Lj,DC}$ in the worst-case scenario (where both BT and EVs are charging/discharging to V_{DC}), have to carry the total power for both BT and EV ports. Thus, average primary side inductor currents are the sum:

$$
I_{Lj,\mathrm{DC(avg)}} = \frac{I_{\mathrm{BT}} + \sum_{j=1}^{N}\frac{V_{\mathrm{EV},j}\cdot I_{\mathrm{EV},j}}{V_{\mathrm{BT}}}}{3\cdot D_1}. \tag{6}
$$

Then, the instantaneous $I_{Lj,DC}(t)$ currents are calculated as follows:

$$I_{Lj,\mathrm{DC}}(t) = \begin{cases} I_{Lj,\mathrm{DC(min)}} + \dfrac{V_{\mathrm{DC}}}{L_{j,\mathrm{DC}}}(t+\alpha) \\ \qquad \text{for } -\alpha < t < T(1-D_1) - \alpha \\ I_{Lj,\mathrm{DC(max)}} - \dfrac{V_{\mathrm{DC}}}{L_{j,\mathrm{DC}}}\left(\dfrac{1}{D_1} - 1\right)(t+\alpha - T(1-D_1)) \\ \qquad \text{for } T(1-D_1) - \alpha < t < T - \alpha \end{cases}, \tag{7}$$

where:

$$I_{Lj,\mathrm{DC(max)}} = I_{Lj,\mathrm{DC(avg)}} + 0.5V_{\mathrm{DC}} \cdot \frac{T(1-D_1)}{L_{j,\mathrm{DC}}},$$

$$I_{Lj,\mathrm{DC(min)}} = I_{Lj,\mathrm{DC(avg)}} - 0.5V_{\mathrm{DC}} \cdot \frac{T(1-D_1)}{L_{j,\mathrm{DC}}}.$$

The formulas above allow not only the selection of appropriate semiconductors but also a comparison of the CF-MAB converter with existing solutions. For example, it can be compared with an architecture in which the storage battery is connected to the DC traction grid via a three-phase interleaved boost converter, while three EV chargers are implemented as independent single-phase DAB converters operating with SPS modulation and connected at their inputs to the BT port. If power delivered to all ports is considered the same, the independent connection of the converters has, on average lower RMS currents in switches, due to some disadvantages of the CF-MAB described earlier (lower transformer utilization and increased S_j, S'_j, S_k, S'_k RMS currents). On the other hand, the RMS current does not fully reflect the differences between the solutions, because the CF-MAB and independent connection of converters differ in the number of switches ($6N$ vs $8N + 6$). To account for this, a total device rating (TDR) coefficient is used, which considers both the number of switches and their electrical stress (i.e., peak voltage and RMS current):

$$\mathrm{TDR} = \sum_{k=1}^{z} V_k\mathrm{d}s \cdot I_k\mathrm{rms}, \tag{8}$$

where $V_k\mathrm{d}s$ is the maximum drain-source voltage of the k-th transistor, and $I_k\mathrm{rms}$ is its RMS current.

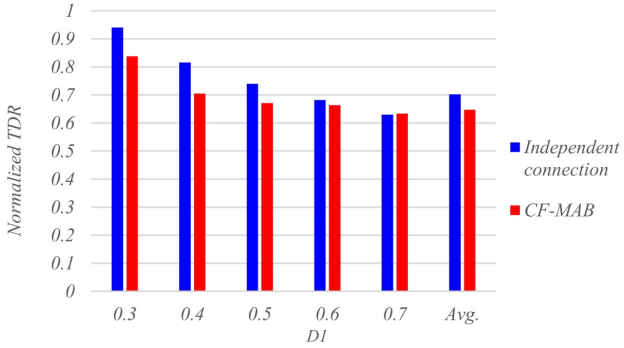


Fig. 3. Comparison of the TDR ratings of the proposed five-port CF-MAB converter and an equivalent converter arrangement comprising a three-phase interleaved boost converter for BT charging and three standalone single-phase DAB converters supplied from the BT port

The results (Fig. 3) show that in all cases, the CF-MAB converter has a lower TDR (10% on average), mostly due to the reduced number of switches. This suggests that the CF-MAB could potentially be less costly than an independent connection of similar converters.

2.3. Main magnetics derivation

The primary-side boost inductor value $L_{j,\mathrm{DC}}$ is determined by the maximum allowable ripple r for the specified maximum power $P_{\mathrm{DC(max)}}$:

$$L_{j,\mathrm{DC(CF-MAB)}} \geq \frac{3 \cdot V_{\mathrm{DC(max)}}^2 \left(1 - \dfrac{V_{\mathrm{DC(max)}}}{V_{\mathrm{BT(min)}}}\right)}{r \cdot P_{\mathrm{DC(max)}} \cdot f_{\mathrm{sw}}}, \tag{9}$$

where $P_{\mathrm{DC(max)}} = P_{\mathrm{BT(max)}} + N \cdot P_{\mathrm{EV},j\mathrm{(max)}}$, N-number of EV ports.

When it comes to $L_{P,j}$ value, it must be low enough to deliver desired peak power $P_{\mathrm{EV},j\mathrm{(max)}}$ to the output during the worst-case scenario and maximum desired phase shift $\delta_{j\mathrm{(max)}}$. Usually, for DAB converters $|\delta_{j\mathrm{(max)}}| \approx \pi/6$:

$$L_{P,j\mathrm{(CF-MAB)}} \leq \frac{V_{\mathrm{EV},j\mathrm{(min)}} V_{\mathrm{BT},j\mathrm{(min)}}}{2n \cdot \pi \cdot f_{\mathrm{sw}} \cdot P_{\mathrm{EV},j\mathrm{(max)}}} \delta_{j\mathrm{(max)}} \left(\frac{2}{3} - \frac{|\delta_{j\mathrm{(max)}}|}{2\pi}\right). \tag{10}$$

The analytically derived Eq. (10) is accurate only for a specific range of ($|\delta_{j\mathrm{(max)}}| < 2\pi(1/3 - D_1) \cup 0 < |\delta_{j\mathrm{(max)}}| < 2\pi(D_1 - 1/3)$) and SPS modulation. Outside this range, the equation changes slightly due to variations in $d_{P,j}$ and the transformer current waveform change. This leads to an increase in the minimum $L_{P,j}$ value or, alternatively, higher phase shift $|\delta_{j\mathrm{(max)}}|$ to achieve the desired power. For equations covering all converter operating regions and for operation with modified DPS modulation, please refer to reference [14].

3. MAB converter control algorithm

The proposed CF-MAB converter is governed by a state-machine-based control algorithm, in which each operating state determines whether the BES and EVs are charging, discharging or remain idle. The charging and discharging limits of both the BES and EVs are established using a voltage-droop strategy based on the catenary voltage measured at the point of common coupling (PCC) of the charging station. This approach was selected due to its low implementation complexity, high reliability and independence from communication with the traction substation or neighboring charging stations connected to the same DC traction network. A detailed description of the high-level energy management algorithm is provided in [5]. Eventually, the high-level control generates the reference currents $I_{\mathrm{BT}}^{\mathrm{ref}}$ and $I_{\mathrm{EV},j}^{\mathrm{ref}}$, which are subsequently tracked by the low-level control system.

The reference currents $I_{\mathrm{BT}}^{\mathrm{ref}}$ and $I_{\mathrm{EV},j}^{\mathrm{ref}}$ are the input for the low-level control system (Fig. 4). The battery storage (BT) is operated around an intermediate state of charge by the balancing strategy described in [15], thereby preserving sufficient energy capacity for both charging and discharging. As shown in Fig. 4, the battery current I_{BT} is controlled by a single PI regulator, which adjusts the input-side duty cycle D_1 according to the error between the measured current and its reference value $I_{\mathrm{BT}}^{\mathrm{ref}}$.

Each EV port employs the conventional constant-current/constant-voltage (CC/CV) charging strategy widely adopted in EV charging systems. The control structure consists of cascaded voltage and current loops. The outer voltage controller compares the measured voltage $V_{\mathrm{EV},j}$ with its reference $V^{\mathrm{ref}}_{\mathrm{EV},j}$ and generates the current reference for the inner loop. Subsequently, the inner current controller regulates the measured current $I_{\mathrm{EV},j}$ to its reference by determining the corresponding phase shift δ_j. This cascaded architecture enables a seamless transition between CC and CV operating modes. During the transition from charging to discharging, the polarities of $V^{\mathrm{ref}}_{\mathrm{EV},j}$ and $V_{\mathrm{EV},N}$ are inverted, forcing the output of the voltage controller to become negative and ensuring the correct operation of the subsequent current-reference saturation block.

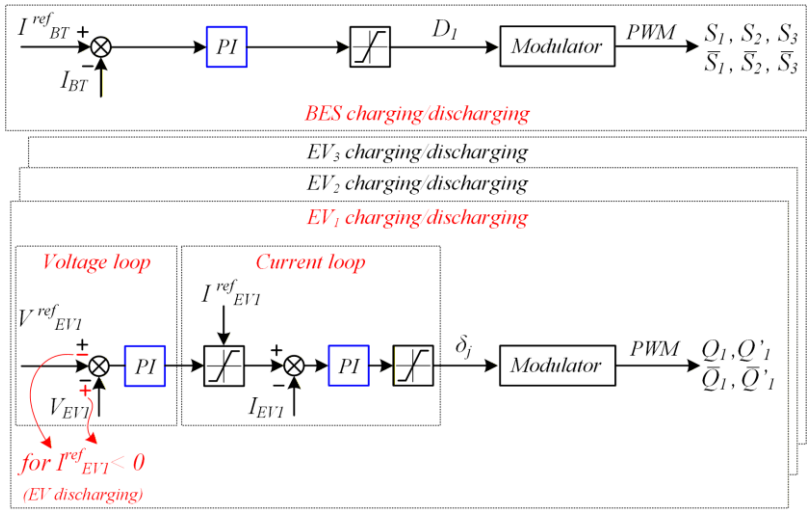


Fig. 4. Closed-loop low-level control of the CF-MAB converter

4. Experimental verification

To verify converter operation, a smaller-scale prototype was assembled with the components specified in Fig. 5 and Fig. 6, and parameters from Table 1.

Table 1. CF-MAB converter prototype parameters

Parameter	Value
DC grid voltage range V_{DC}	200–450 V
Battery voltage V_{BT}	600 V
EVs voltage range $V_{\mathrm{EV},1}$, $V_{\mathrm{EV},2}$, $V_{\mathrm{EV},3}$	250–350 V

Continued on next page

Table 1 – *Continued from previous page*

Parameter	Value
Transformer ratio n_s/n_p	0.5
Primary side turns number n_p	28
Secondary side turns number n_s	14
Transformer magnetizing inductance	45 mH
Transformer leakage inductance	10 μH
DC side inductance $L_{1,\mathrm{DC}}$, $L_{2,\mathrm{DC}}$, $L_{3,\mathrm{DC}}$	490 μH
$L_{1,\mathrm{DC}}$, $L_{2,\mathrm{DC}}$, $L_{3,\mathrm{DC}}$ number of turns	23
Primary transformer inductors $L_{P,1}$, $L_{P,2}$, $L_{P,3}$	100 μH
$L_{P,1}$, $L_{P,2}$, $L_{P,3}$ number of turns	11
Inductors $L_{1,\mathrm{DC}}$, $L_{2,\mathrm{DC}}$, $L_{3,\mathrm{DC}}$, $L_{P,1}$, $L_{P,2}$, $L_{P,3}$ air gap	4 mm
Battery side capacitor $C_{f,\mathrm{BT}}$	2×420 μH
Battery and EV sides inductances $L_{f,\mathrm{BT}}$, $L_{f,\mathrm{EV}}$	10 μH
EV and DC side capacitors $C_{f,\mathrm{EV}}$, $C_{f,\mathrm{DC}}$	420 μF
Filter inductance $L_{f,\mathrm{DC}}$	10 μH
Switching frequency f_{sw}	25 kHz



Fig. 5. Developed full bridge module, used for converter assembly (a), and converter magnetics (b) for the input-side three-phase full bridge, the same modules are used as in (a), but with 3 transistor half-bridge modules

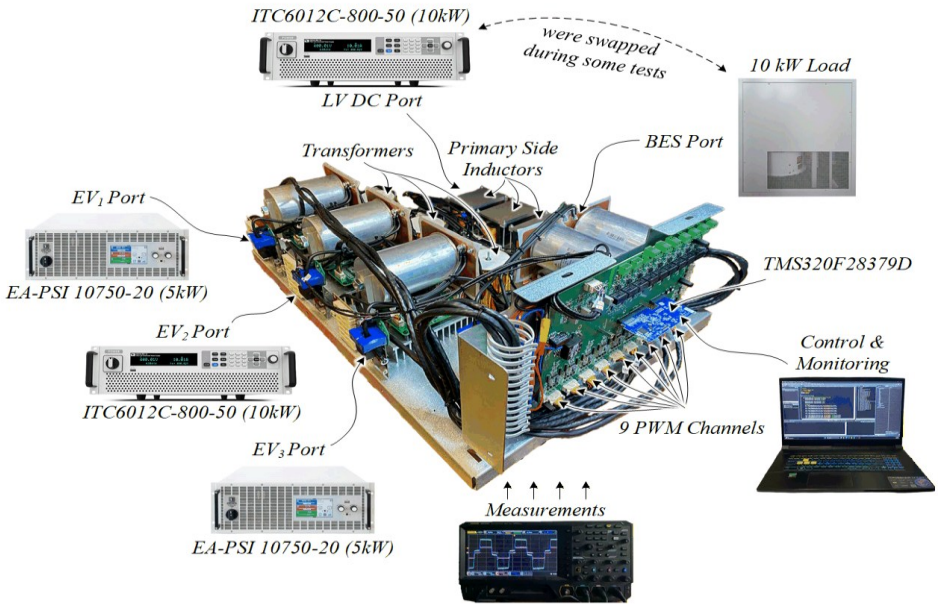


Fig. 6. Assembled CF-MAB converter prototype, tested at up to 10 kW, and the equipment used

The experimental validation presented in this section was performed using SPS modulation. Throughout the reported tests, the battery-side voltage V_{BT} was kept fixed. This assumption is representative of practical operation because the battery terminal voltage typically evolves on a much slower timescale and is predominantly determined by its state of charge. The DC-side voltage V_{DC} on the other hand, was adjusted to reproduce the voltage fluctuations that can occur in a DC traction network. Different voltage and power references were also applied to the individual EV ports, allowing the converter behavior and associated waveforms to be examined over a range of port operating conditions.

Figure 7 summarizes the principal measured waveforms for the three EV branches. These include the DC-side inductor currents $I_{L1\mathrm{DC}}$, $I_{L2\mathrm{DC}}$ and $I_{L3\mathrm{DC}}$, primary side-voltages $V_{P,1}$, $V_{P,2}$, $V_{P,3}$, secondary-side voltages $V_{S,1}$, $V_{S,2}$ and $V_{S,3}$ and the corresponding transformer-inductor currents $I_{LP,1}$, $I_{LP,2}$ and $I_{LP,3}$.

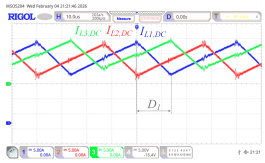
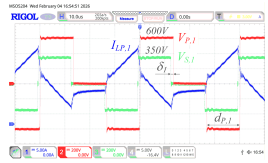
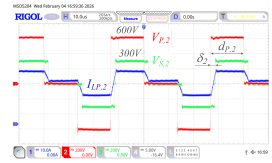
	V_{BT} = 600 V, P_{BT} = 4 kW, V_{DC} = 200 V, D_1 = 0.33, $d_{P,j} = d_{S,j} = T/3 = 13.33\ \mu$s	V_{BT} = 600 V, P_{BT} = 4 kW, V_{DC} = 300 V, D_1 = 0.50, $d_{P,j} = d_{S,j} = T/3 = 13.33\ \mu$s	V_{BT} = 600 V, P_{BT} = 4 kW, V_{DC} = 450 V, D_1 = 0.75, $d_{P,j} = d_{S,j} = T(1-D_1) = 10\ \mu$s
			

Figure continued on next page

Figure continued from the previous page

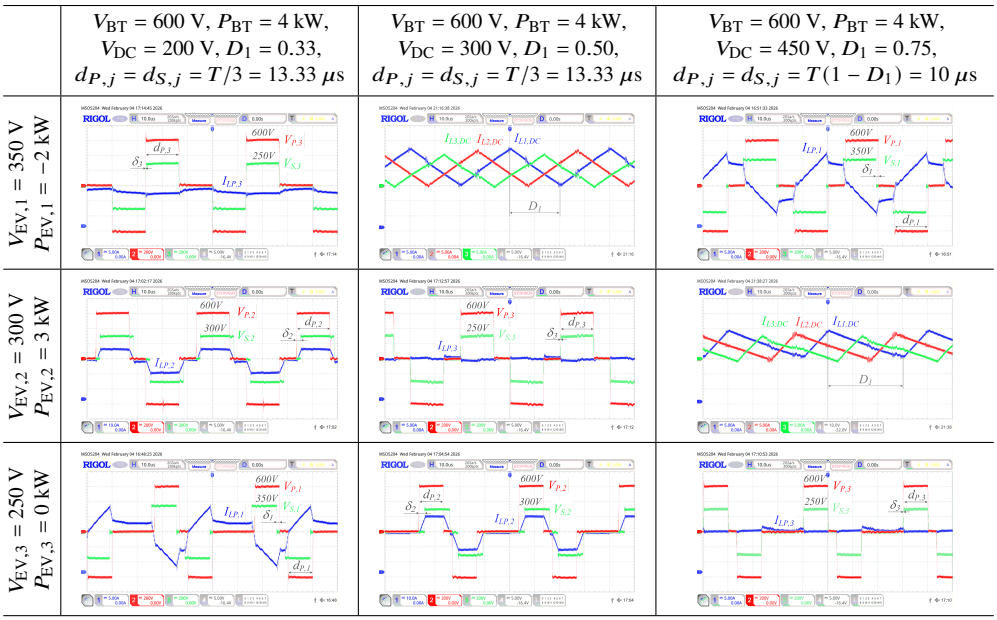


Fig. 7. Measured waveforms of the converter operation for different operating conditions. Battery port voltage V_{BT} in all cases was held constant, as in a practical application, it does not change fast and depends on SOC. Converter operation is shown for different DC-grid V_{DC} voltage, which represents changes of traction grid voltage, that usually occur in real operating conditions. The power and voltage of each EV are also different, to show how operating waveforms change during different conditions. The EV_3 port power is zero and EV_3 is disconnected by the relay, but still, current flows through a transformer

For the first test point, the DC-grid voltage was relatively low, giving a duty ratio of $D_1 = V_{DC}/V_{BT} = 1/3$, corresponding to a low DC traction grid voltage. This value corresponds to the limiting case for which $d_{P,j} = d_{S,j} = T/3$. Consequently, the primary and secondary transformer voltages $V_{P,j}$ and $V_{S,j}$ contain a zero-voltage interval on only one side of each waveform. If the voltage ratio were reduced further, both $d_{P,j}$ and $d_{S,j}$ would become shorter.

At this operating point, 4 kW was transferred to the BT port. EV1 supplied 2 kW to the converter, i.e., $P_{EV,1} = -2$ kW with $\delta_1 < 0$ while EV2 absorbed 3 kW, corresponding to $P_{EV,2} = 3$ kW and $\delta_2 > 0$. EV3 did not exchange active power, since $\delta_3 = 0$ and $P_{EV,3} = 0$ kW. Hence, part of the energy delivered by EV1 was directly utilized by EV2. From the overall power balance, the DC-grid port therefore supplied $P_{DC} = P_{BT} + P_{EV,1} + P_{EV,2} + P_{EV,3} = 5$ kW. The measured average value of each DC-side inductor current $I_{Lj,DC}$ was approximately 8.5 A.

The experimental waveforms also confirm the behavior anticipated from the analytical model. For EV1, the mismatch between V_{BT} and V_{EV1} produces a significant current gradient $\mathrm{d}i/\mathrm{d}t$ over the $d_{P,1} - \delta_1$ intervals. As a result, the transformer RMS current becomes higher, the port-current ripple increases and additional EMI may be generated. The EV2 branch behaves differently because its voltage levels approximately fulfill the matching relation $V_{BT} = V_{EV,2}/n$. The transformer current therefore changes very little during the corresponding $d_{P,2} - \delta_2$ intervals. A small circulating current can also be identified in the EV3 transformer despite the absence of active power transfer and the disconnection of this port through its relay. This current originates from the repetitive

charge and discharge processes associated with the EV3 output-filter capacitor $C_{f,\mathrm{EV3}}$. One possible way of suppressing this no-load circulation would be to stop switching the semiconductor devices assigned to an inactive port. The drawback is that reconnecting an EV would then require the complete port startup sequence to be performed before charging could resume once again.

The second experimental point corresponds to $D_1 = 0.5$, obtained with $V_{\mathrm{DC}} = 300$ V and $V_{\mathrm{BT}} = 600$ V. At this voltage ratio, the non-zero durations of both transformer-side voltage waveforms attain their maximum values, such that $d_{P,j} = d_{S,j} = T/3$. In contrast to the first operating point, the resulting $V_{P,j}$ and $V_{S,j}$ waveforms possess odd symmetry and the zero-voltage intervals are distributed symmetrically on the two sides of each waveform.

Finally, the third operating point considers a considerably larger difference between the DC-grid and battery voltages, producing $D_1 = 0.75$. In this region, the available non-zero transformer-voltage duration decreases according to $d_{P,j} = d_{S,j} = T(1 - D_1)$. The shorter effective voltage intervals reduce the amount of power that can be transferred for a given phase shift. Therefore, achieving power levels comparable to those of the preceding cases requires greater phase shifts for EV1 and EV2. However, such an extreme voltage ratio is not expected during typical system operation. It could arise only under an unfavorable combination of conditions, for example when the traction-grid voltage stabilization functionality is inactive while the battery voltage is simultaneously close to one of its operating limits.

The converter efficiency was experimentally assessed across a range of operating conditions, including different power levels, operating modes and directions of power transfer. The reported efficiency accounts for the overall losses of the experimental setup rather than the converter losses alone. These include conduction losses in the cables connecting the converter ports to the power supplies and loads, together with the power required by the control circuitry. For all considered test cases, the achievable power level was constrained by the maximum output and absorption capabilities of the laboratory power supplies.

When only the BT port operates and the power of the EV ports is zero $P_{\mathrm{EVs}} = 0$, efficiency is highest at a high input voltage ($V_{\mathrm{DC}} = 450$ V), due to lower input current and reduced ohmic losses (Fig. 8). However, when power is delivered only to EVs and $P_{\mathrm{BT}} = 0$, the situation reverses: the lowest

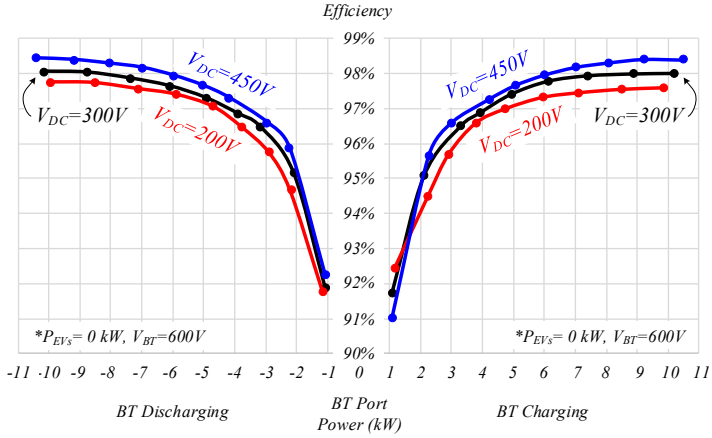
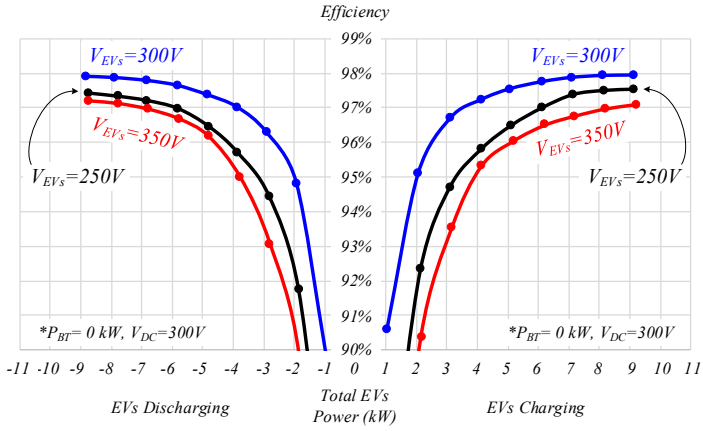
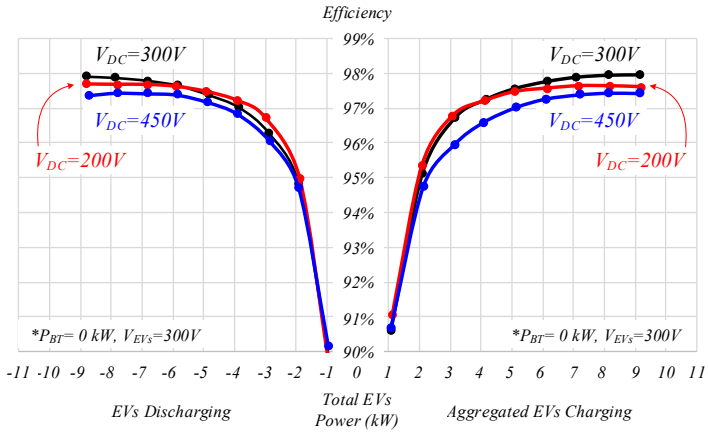


Fig. 8. Efficiency curves for zero EVs charging power $P_{\mathrm{EVs}} = 0$ kW and different DC grid voltage V_{DC}

efficiency occurs at $V_{\mathrm{DC}} = 450$ V (Fig. 9(b)), because of lower $d_{P,j}$, reduced transformer utilization and increased transformer RMS currents. The highest efficiency is achieved when the battery voltage $V_{\mathrm{BT}} = 600$ V matches $V_{\mathrm{EVs}} = 300$ V using a transformer with a ratio of $n_s/n_p = 0.5$ (Fig. 9(a)).



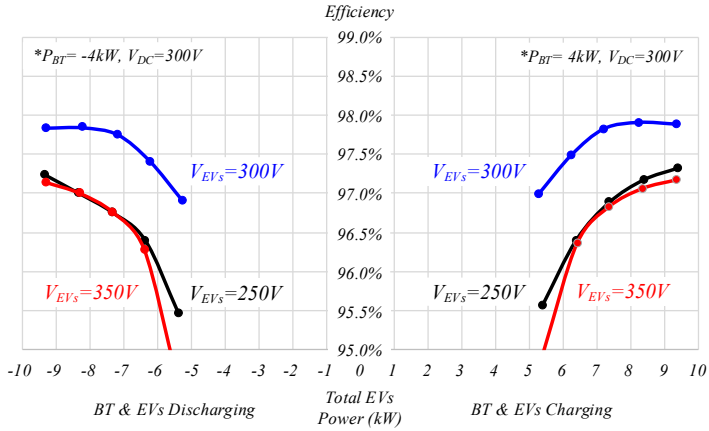
(a)



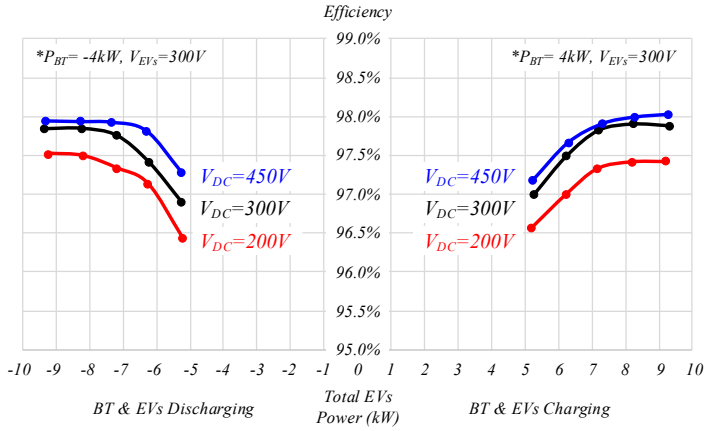
(b)

Fig. 9. Efficiency curves for zero BT charging power $P_{\mathrm{BT}} = 0$ kW and different V_{EVs} voltages, while DC grid voltage is constant $V_{\mathrm{DC}} = 300$ V (a), as well as different DC grid voltage V_{DC} while the voltage of all EVs is the same and equals $V_{\mathrm{EVs}} = 300$ V (b). Power is equally shared between 3 EV ports

When both EV and BT ports are loaded and $V_{\mathrm{DC}} = 300$ V, the highest efficiency occurs for $V_{\mathrm{EVs}} = 300$ V, because the EV-port voltages are matched with the battery voltage. For $V_{\mathrm{EVs}} = 250$ V or 350 V, transformer circulating currents increase and efficiency drops by about 1% (Fig. 10(a)). In Fig. 10(b), the low EV-port efficiency at $V_{\mathrm{DC}} = 450$ V is compensated by high input-side efficiency, keeping the overall efficiency high.



(a)



(b)

Fig. 10. Efficiency curves when both the EVs and BT are charging or discharging for different EV voltage levels, while DC grid voltage is constant V_{DC} = 300 V (a), and different DC grid voltage levels, while the voltage of all EVs is the same and equals V_{EVs} = 300 V (b). Charging and discharging power of the BT port in all cases is constant and equal to P_{BT} = ±4 kW, where the sign depends on whether battery is charging or discharging

5. Conclusions

Experimental verification of the converter has shown its ability to independently deliver power to any port, without affecting the power of other ports, which in practice means that BT and EVs can be independently charged, discharged and their power level can be regulated without affecting other ports, which distinguishes the studied converter from typical Multi-Active Bridge converters with a common transformer core. The converter has shown a high efficiency of 98% peak at 9.5 kW, when EV voltages V_{EVs} = 300 V is matched with the BT voltage V_{BT} = 600 V using a transformer

with $n = 0.5$. During the mismatch, when $V_{EVs} = 250$ V or $V_{EVs} = 350$ V, efficiency is reduced due to increased transformer and switch RMS currents. Despite increased RMS currents and reduced transformer utilization ratio, the multiport CF-MAB converter shows, on average, ~10% reduced total device rating in comparison to conventional solution with independent converters, due to the lower number of transistors required to connect BT and N EVs into the LV DC traction grid. This makes it a promising solution to be used in a multiterminal urban EV fast charging station, where several EV charging stations are located close to each other.

Acknowledgements

This research was funded by the EU Horizon 2020 Framework Programme Project: 955614-SMARTGY-sum–H2020-MSCA-ITN-2020 and partially realized under the Intelligent Development Operational Program 2014–2020 co-financed by the European Regional Development Fund – agreement within NCBiR project No: POIR.01.01.01-00-1399/20-00 "Self-adaptive fast and ultra-fast charging systems for electric vehicles using Cubic System technology".

References

[1] Weisbach M., Schneider T., Maune D., Fechtner H., Spaeth U., Wegener R., Soter S., Schmuelling B., *Intelligent Multi-Vehicle DC/DC Charging Station Powered by a Trolley Bus Catenary Grid*, Energies, vol. 14, no. 24, 8399 (2021), DOI: 10.3390/en14248399.

[2] Husev O., Vinnikov D., Kouro S., Blaabjerg F., Roncero-Clemente C., *Dual-Purpose Converters for DC or AC Grid as Energy Transition Solution: Perspectives and Challenges*, IEEE Industrial Electronics Magazine, vol. 18, no. 1, pp. 46–57 (2024), DOI: 10.1109/MIE.2022.3230219.

[3] Tian G., Zhou G-H., Li H., Yang Y-H., Zhou D., *Symmetrical Bipolar Output Isolated Four-Port Converters Based on Center-Tapped Winding for Bipolar DC Bus Applications*, IEEE Transactions on Power Electronics, vol. 37, no. 2, pp. 2338–2351 (2022), DOI: 10.1109/TPEL.2021.3107154.

[4] Krueger H., Fletcher D., Cruden A., *Vehicle-to-Grid (V2G) as line-side energy storage for support of DC-powered electric railway systems*, Journ. of Rail Transp. Plan. & Manag., vol. 19, 100263 (2021), DOI: 10.1016/j.jrtpm.2021.100263.

[5] CENELEC, *Railway Applications—Supply Voltages of Traction Systems*, EN 50163:2004+A3:2022 (2022).

[6] CENELEC, *Railway Applications—Fixed Installations and Rolling Stock—Technical Criteria for the Coordination Between Electric Traction Power Supply Systems and Rolling Stock to Achieve Interoperability—Part 1: General*, EN 50388-1:2022 (2022).

[7] Buticchi G., Costa L.F., Barater D., Liserre M., Amarillo E.D., *A Quadruple Active Bridge Converter for the Storage Integration on the More Electric Aircraft*, IEEE Transactions on Power Electronics, vol. 33, no. 9, pp. 8174–8186 (2018), DOI: 10.1109/TPEL.2017.2781258.

[8] Bandyopadhyay S., Qin Z., Bauer P., *Decoupling Control of Multiactive Bridge Converters Using Linear Active Disturbance Rejection*, IEEE Transactions on Industrial Electronics, vol. 68, no. 11, pp. 10688–10698 (2021), DOI: 10.1109/TIE.2020.3031531.

[9] Böhler J., Krismer F., Sen T., Kolar J.W., *Optimized Modulation of a Four-Port Isolated DC–DC Converter Formed by Integration of Three Dual Active Bridge Converter Stages*, 2018 IEEE International Telecommunications Energy Conference (INTELEC), Turino, Italy, pp. 1–8 (2018), DOI: 10.1109/INTLEC.2018.8612312.

[10] Uno M., Sato M., Tada Y., Iyasu S., Kobayashi N., Hayashi Y., *Partially Isolated Multiport Converter With Automatic Current Balancing Interleaved PWM Converter and Improved Transformer Utilization for EV Batteries*, IEEE Transactions on Transportation Electrification, vol. 9, no. 1, pp. 1273–1288 (2023), DOI: 10.1109/TTE.2022.3175032.

[11] Su G.-J., Tang L., *A Reduced-Part, Triple-Voltage DC–DC Converter for EV/HEV Power Management*, IEEE Transactions on Power Electronics, vol. 24, no. 10, pp. 2406–2410 (2009), DOI: 10.1109/TPEL.2009.2026989.

[12] Wang Z., Li H., *A Soft Switching Three-phase Current-fed Bidirectional DC–DC Converter with High Efficiency Over a Wide Input Voltage Range*, IEEE Transactions on Power Electronics, vol. 27, no. 2, pp. 669–684 (2012), DOI: 10.1109/TPEL.2011.2160284.

[13] Strzelecki R., Lukianov M., *Multi-station system for electric vehicle charging stations*, Poland Patent P.448300 (in Polish), April 2024 [online], available at: https://ewyszukiwarka.pue.uprp.gov.pl/search/search-results/b1b5d54c-35d9-4afd-b70f-ed233ecad50b, accessed Jun. 13, 2026.

[14] Lukianov M., Derkacz P., Strzelecki R., *Multi Active Bridge converter with DPS modulation for bidirectional EV charging from DC traction grid*, IECON 2024 - 50th Annual Conference of the IEEE Industrial Electronics Society, Chicago, IL, USA pp. 1–7 (2024), DOI: 10.1109/IECON55916.2024.10905342.

[15] Lukianov M., Cadaval E.R., Matiushkin O., Strzelecki R., *Traction powered multiport DC–DC converter for bidirectional EV charging application – HIL simulation results*, 2025 IEEE 19th International Conference on Compatibility, Power Electronics and Power Engineering (CPE-POWERENG), Antalya, Turkiye, pp. 1–6 (2025), DOI: 10.1109/CPE-POWERENG63314.2025.11027251.